

Specific Heat Anomalies and Local Symmetry Breaking in (Anti-)Fluorite Materials: A Machine Learning Molecular Dynamics Study

Keita Kobayashi,^{1,*} Hiroki Nakamura,¹ Masahiko Okumura,¹ Mitsuhiro Itakura,¹ and Masahiko Machida¹

¹*CCSE, Japan Atomic Energy Agency, 178-4-4, Wakashiba, Kashiwa, Chiba 277-0871, Japan*

(Dated: December 17, 2024)

Understanding the high-temperature properties of materials with (anti-)fluorite structures is crucial for their application in nuclear reactors. In this study, we employ machine learning molecular dynamics (MLMD) simulations to investigate the high-temperature thermal properties of thorium dioxide, which has a fluorite structure, and lithium oxide, which has an anti-fluorite structure. Our results show that MLMD simulations effectively reproduce the reported thermal properties of these materials. A central focus of this work is the analysis of specific heat anomalies in these materials at high temperatures, commonly referred to as Bredig, pre-melting, or λ -transitions. We demonstrate that a local order parameter, analogous to those used to describe liquid-liquid transitions in supercooled water and liquid silica, can effectively characterize these specific heat anomalies. The local order parameter identifies two distinct types of defective structures: lattice defect-like and liquid-like local structures. Above the transition temperature, liquid-like local structures predominate, and the sub-lattice character of mobile atoms disappears.

I. INTRODUCTION

Uranium, plutonium, and thorium dioxides (UO_2 , PuO_2 , and ThO_2), which exhibit fluorite structures, are representative nuclear fuel materials. Lithium oxide (Li_2O), with anti-fluorite structure, is a candidate material for tritium breeding for nuclear fusion reactor [1]. In both cases, understanding the material properties over a wide range of temperatures is essential for reactor design and ensuring nuclear safety.

Atomic simulations, such as molecular dynamics (MD) simulations [2–9] and density functional theory (DFT) calculations [10–15], are effective tools for complementing experimental data and unraveling phenomena that remain unresolved at the atomic level. Among these methods, machine learning molecular dynamics (MLMD) simulations [16–19] are particularly well-suited for investigating the high-temperature properties of materials. In MLMD, flexible functions with multiple adjustable parameters, such as artificial neural networks [16, 18] and Gaussian processes [17, 19], are employed as the interatomic potentials for MD simulations. These interatomic potentials, trained to imitate the DFT potential energy surface accurately, are referred to as machine learning potentials (MLPs). MLMD simulation enables accurate and large-scale MD simulations with near DFT accuracy. Currently, MLMD simulations are extensively utilized for simulating various systems [20–22], including nuclear fuels [23–25]. In this study, we employ MLMD simulations to investigate the high-temperature properties of nuclear materials with (anti-)fluorite structures.

One of the significant phenomena of (anti-)fluorite materials at high temperature is specific heat anomaly, known as the λ -transition, Bredig transition, or pre-melting phase transition [26]. In a fluorite structure, the

4a and 8c positions are occupied by cations and anions, respectively (see Fig.1). Conversely, in an anti-fluorite structure, the 4a and 8c positions are occupied by anions and cations, respectively. The specific heat anomaly of (anti-)fluorite materials is considered to be attributed to the disorder of 8c position atoms, the formation of Frenkel pair like defects [27–29] at high temperature. However, the diffusion of mobile atoms is highly cooperative and complex. The dynamics of the mobile atoms in fluorite materials exhibit string-like atomic diffusion [30, 31], which is observed in glass-forming system [32]. The ionic conductivity of fluorite materials exhibits a rapid increase with rising temperature, leveling off at a value indistinguishable from that of the liquid state above the λ -transition temperature [33, 34]. The highly cooperative and liquid-like fast atomic diffusion near the λ -transition temperature complicates the characterization of defect structures in (anti-)fluorite materials within the framework of lattice defects.

In this paper, we investigate the high-temperature properties of ThO_2 (fluorite structure) and Li_2O (anti-fluorite structure) using MLMD simulations, with a focus on characterizing their heat anomalies from the perspective of local symmetry breaking. First, we construct MLPs for ThO_2 and Li_2O . Using a farthest-point sampling method [35, 36] and evaluating the uncertainty in the DFT reference data, we generate 1,000 DFT reference data and create MLPs for both ThO_2 and Li_2O . The ThO_2 -MLP created from these 1,000 DFT data achieves almost the same accuracy as the previously developed model [23] and well reproduces experimental data. Similarly, the Li_2O -MLP accurately reproduces reported experimental properties, such as lattice constants, thermal expansion coefficients, Frenkel pair formation energy, and melting temperature. We also discuss the λ -peak of specific heat capacity and its corresponding temperature for Li_2O , which have not been experimentally measured. Next, using the MLMD trajectories for ThO_2 and Li_2O , we examine the defective structures contributing

* kobayashi.keita@jaea.go.jp

to the specific heat anomalies. We focus on the similarities between the specific heat anomalies of (anti-) fluorite structures and a liquid-liquid phase transition in network-forming liquids such as supercooled water and liquid silica [37–39]. These systems also exhibit a λ -peak of specific heat capacity due to their local symmetry breaking of a local tetrahedral structure. For ThO_2 and Li_2O , we formulate the heat anomalies from the perspective of local symmetry breaking within octahedral structures, which represent the minimal locally ordered arrangements of mobile atoms. The defect structures in ThO_2 and Li_2O below and above the λ -transition temperature are characterized by changes in the distribution of the octahedral local order parameter.

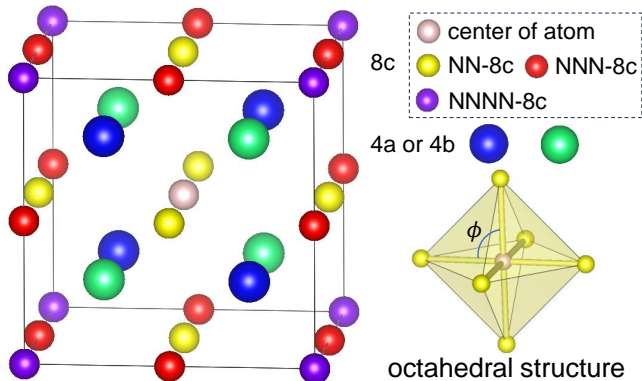


FIG. 1. Wyckoff positions of the (anti-)fluorite structure with space group $\text{Fm}\bar{3}\text{m}$. Thorium and oxygen atoms occupy the 4a (green sphere) and 8c positions (white, yellow, red, and purple spheres) in ThO_2 , while lithium and oxygen atoms occupy the 8c and 4a positions in Li_2O , respectively. The 4b position is an interstitial site. NN-8c, NNN-8c, and NNNN-8c mean the nearest neighboring 8c, next-nearest neighboring 8c, and next-next-nearest neighboring 8c positions from the center of an 8c position. The octahedral structure represented by a yellow polygon denotes the minimal local order for oxygen in ThO_2 and lithium in Li_2O .

II. METHOD

To construct a machine learning potential (MLP), it is necessary to prepare a diverse set of DFT reference data. We employed classical MD simulations to generate various structural configurations of ThO_2 and Li_2O . In this paper, all MD simulations are carried out by LAMMPS [40]. For ThO_2 , the Cooper, Rushton, and Grimes (CRG) potential was utilized [3], while for Li_2O , the Asahi potential was used [8]. NPT simulations were performed for ThO_2 over a temperature range of 100 K to 5000 K with a 200 K temperature step, and for Li_2O from 100 K to 2500 K with a 100 K temperature step. The $2 \times 2 \times 2$ and $3 \times 3 \times 3$ supercell structures (96 and 324 atoms, respectively) were used for the NPT simulations. At each temperature step, an NPT simulation

with 100,000 time steps was executed, collecting structural data at intervals of 100 steps. Consequently, the structures of ThO_2 and Li_2O generated through classical MD were each 50,000 structures. From these configurations, important structures were selected using a farthest-point sampling (FPS) methodology [35, 36]. Initial structures for FPS were selected from perfect crystals at low temperatures. Subsequent configurations were selected according to the following criteria:

$$k = \underset{k \in K}{\operatorname{argmax}}(\min_{j \in J} |\Phi_k - \Phi_j|), \quad (1)$$

where Φ represents structural descriptor, $|\cdot|$ is the Euclidean distance, J denotes the set of already selected structures and K represents the set of structures yet to be selected. We constructed the structural descriptor of ThO_2 and Li_2O as $\Phi_m = \frac{1}{N_m} \bigoplus_{\alpha} \left(\sum_{i_{\alpha}} \mathbf{G}_{i_{\alpha}}^{(m)} \right)$, where N_m is a number of atoms for m -th structure, α denotes the chemical species ($\alpha = \text{O}, \text{Th}$ or Li), and $\mathbf{G}_{i_{\alpha}}$ represents i_{α} -th local atomic environmental descriptor. The following symmetry functions [16, 18] were adopted as the local atomic environmental descriptors:

$$\mathbf{G}_i = \mathbf{G}_{\text{R},i} \oplus \mathbf{G}_{\text{A},i}, \quad (2)$$

$$\mathbf{G}_{\text{R},i} = \sum_j e^{-\eta_{\text{R}}(R_{ij} - R_s)^2} f_c(R_{ij}), \quad (3)$$

$$\mathbf{G}_{\text{A},i} = 2^{1-\xi} \sum_{j \neq i} \sum_{k \neq i,j} (1 + \lambda \cos \theta_{ijk})^{\xi} e^{-\eta_{\text{A}}(R_{ij}^2 + R_{ik}^2 + R_{jk}^2)} \times f_c(R_{ij}) f_c(R_{ik}) f_c(R_{jk}), \quad (4)$$

with the cutoff function

$$f_c(R) = \begin{cases} 0.5 \cos\left(\frac{\pi R}{R_c} + 1\right) & \text{for } R \leq R_c \\ 0 & \text{for } R_c < R \end{cases}, \quad (5)$$

where R_{ij} is the distance between the i -th and j -th atoms, θ_{ijk} is the angle formed by line segments between the i - j -th and the i - k -th atom bonds. We utilized the previous parameterization of symmetry functions ($R_c, \eta_{\text{R}}, \eta_{\text{A}}, R_s, \lambda$, and ζ) for ThO_2 [23]. For Li_2O , the cutoff radius R_c for $\mathbf{G}_{\text{R},i}$ and $\mathbf{G}_{\text{A},i}$ were taken as 6.5 Å. The other parameters of symmetry functions for Li_2O were selected by CUR decomposition [35]. Using FPS with the structural descriptor Φ_m , we selected 100 configurations from 50,000 structures for both ThO_2 and Li_2O using FPS.

We conducted DFT calculations for the 100 configurations selected by FPS. The Vienna Ab-initio Simulation Package (VASP) [41, 42] was utilized for these calculations. In all calculations, the projector-augmented wave (PAW) method [43] was employed, with an energy cutoff of 500 eV. The strongly constrained and appropriately normed (SCAN) meta-GGA exchange-correlation functional [44] was used, since MLP based on the SCAN functional is suitable to reproduce high-temperature thermal properties of ThO_2 [23]. We trained Behler-Parrinello neural networks type MLPs on 100 DFT reference data

sets for ThO₂ and Li₂O using the n2p2 code [45]. The symmetry function defined in Eq.(2) was used as input of the neural network. The neural network architecture consisted of two hidden layers, each with 30 nodes, and hyperbolic tangent activation functions.

By identifying structures with high uncertainty in the MLP outputs for various structures and incorporating these structures into the DFT reference data, the overall quality of the reference data can be improved [46–51]. Therefore, using the MLPs created from the 100 DFT reference data sets, we again conducted NPT simulations over a temperature range of 300 to 4500 K (300 to 2500 K) for ThO₂ (Li₂O), to generate various structures. The uncertainty of the MLP outputs was assessed by evaluating the variance of the outputs from multiple MLPs. We divided a set of the 100 DFT reference data, S , into five non-overlapping datasets, $S_{l=1,\dots,5}$, and created five MLPs trained by the 80 DFT reference data from $S \setminus S_l$. Using ensemble of MLPs outputs, we preferentially selected structures that exhibited a large maximum force prediction variance. The maximum force prediction variance was defined as $\text{Var}(\mathbf{F}^{(m)}) \equiv \max_{i_m} \langle |\mathbf{F}_{i_m}^{(m)} - \langle \mathbf{F}_{i_m}^{(m)} \rangle|^2 \rangle$, where $\mathbf{F}_{i_m}^{(m)}$ denotes the force acting on the i_m -th atom in the m -th structure, and the brackets $\langle \cdot \rangle$ represent the ensemble average for outputs of five MLPs. We also selected the structures that had the symmetry functions in the extrapolation region to ensure that the predictions of the MLP remain as interpolative as possible during MLMD simulations. The number of extrapolated symmetry functions was calculated as $N_E^{(m)} = \sum_{i_m} N_m \sum_d^D [1 - H_S(G_{i,d})]$, where N_m is a number of atoms for m -th structure, D denotes the dimension of the symmetry function, $H_S(G_{i,d})$ is a step function indicating whether $G_{i,d}$ is within the symmetry function range of the DFT reference data, S . We selected 900 structures with a large maximum force prediction variance and a large number of extrapolations, incorporating these structures into the DFT reference data. The total numbers of the reference data for ThO₂ and Li₂O used to create MLPs were 1000 structures.

We also created validation data to evaluate the root mean square error (RMSE) of the MLPs. NPT simulations with the MLPs were conducted at temperatures of 300, 1300, 2300, 3300, and 4300 K for ThO₂, and 300, 800, 1300, 1800, and 2300 K for Li₂O. From the trajectory at each temperature, we randomly selected 20 structures and calculated the DFT energy and forces for these structures as validation data. The resulting RMSEs for the ThO₂- and Li₂O-MLPs are summarized in Table I. For the solid phase, the RMSEs of the ThO₂- and Li₂O-MLPs are below 1 meV/atom for energies and 0.12 eV/Å for forces. While the RMSEs for the liquid phase are higher than those for the solid phase, the values are comparable to typical RMSEs reported in previous studies [16, 50, 52–54].

TABLE I. RMSE of ThO₂- and Li₂O-MLP

ThO ₂ -MLP					
number of data	20	20	20	20	20
phase	solid	solid	solid	solid	liquid
T [K]	300	1300	2300	3300	4300
RMSE for energy [meV/atom]	0.109	0.367	0.997	0.851	3.514
RMSE for force [eV/Å]	0.015	0.035	0.063	0.119	0.190
Li ₂ O-MLP					
number of data	20	20	20	20	20
phase	solid	solid	solid	solid	liquid
T [K]	300	800	1300	1800	2300
RMSE for energy [meV/atom]	0.092	0.222	0.287	0.457	4.879
RMSE for force [eV/Å]	0.028	0.027	0.031	0.041	0.245

III. RESULTS AND DISCUSSION

A. Thermal properties of ThO₂ and Li₂O computed by MLMD

TABLE II. Comparison of the physical properties of ThO₂ computed in this study with previous MLMD study and experiments. The lattice constant $L(T)$ at 300 K, the averaged coefficient of linear thermal expansion (ACLTE) in the range from 300 to 1600K, the onset temperature of heat capacity anomaly T_a , λ -transition temperature T_c , and melting point are summarized.

	MLMD		Exp.
	this study (1,000 data)	previous study [23] (7,007 data)	
$L(300\text{K})$ [Å]	5.617	5.624	5.592 [55]
ACLTE [10^{-6}K^{-1}]	10.02	9.71	9.5 [56]
			9.67 [57]
			11.07 [58]
T_a [K]	2460	2460	
T_c [K]	3200	3200	2950 [59]
			3090 [60]
T_m [K]	3610	3610-3620	3651 [59]

First, we demonstrate that the present ThO₂-MLP created with 1,000 data has sufficient performance comparable to the MLP previously developed with 7,007 data set [23]. We conducted MLMD-NPT simulations for ThO₂ using a $6 \times 6 \times 6$ supercell (2592 atoms), with a time step of 2 fs and a total simulation time of 200 ps. Table II summarizes the thermal properties of ThO₂ computed by the present ThO₂-MLP. The lattice constant $L(T)$ at $T = 300$ K obtained by the present MLMD agrees well with the previous MLMD calculation and experimental data [55]. The averaged coefficient of linear thermal expansion (ACLTE), defined by $\text{ACLTE} = \frac{1}{T_2 - T_1} \int_{T_1}^{T_2} \frac{1}{L(T)} \frac{dL(T)}{dT} dT$, in the range from $T_1 = 300$ K to $T_2 = 1600$ K, is also comparable with values reported in the previous study and experimental data [56–58]. Figure 2(a) shows the molar

specific heat capacity, C_p , calculated by MLMD. The specific heat capacity exhibits an anomaly at high temperatures, attributed to the disorder of oxygen atoms. The onset temperature of the specific heat anomaly, T_a , is characterized as the temperature at which the change in entropy, $dS/dT = C_p/T$, reaches a minimum value [61]. The peak position of C_p is defined as the λ -transition temperature. Both T_a and T_c are consistent with previous MLMD results, and T_c is comparable to experimental observations. Finally, the melting point was evaluated using a two-phase simulation approach. A $6 \times 6 \times 12$ supercell (5184 atoms), containing both solid and liquid phases, was used as the initial configuration. MLMD- NPT simulations were conducted at temperatures ranging from 3400 K to 3800 K, with a total simulation time of 500 ps. The melting point, determined from the temperature corresponding to the enthalpy jump, is in excellent agreement with prior results and experimental data (see Fig.2(b) and Table II). In conclusion, the present ThO_2 -MLP, developed with a dataset of 1,000 configurations, is shown to be sufficiently reliable when compared to previous MLMD results and experimental data. Similarly, the Li_2O -MLP, constructed with the same dataset size, is expected to yield reliable predictions for the thermal properties of Li_2O .

Next, we investigate the thermal properties of Li_2O using MLMD simulations. MLMD- NPT simulations were conducted for Li_2O with a time step of 1 fs. The system size and total simulation time were the same as those used in the MLMD calculations for ThO_2 . The lattice constant obtained from the MLMD simulations shows good agreement with the reported experimental data over a wide temperature range [62–64] (see table III and Fig.3(a)). Additionally, the ACLTE computed in the range from 300 to 1280 K also agrees with experimental value [65]. The onset temperature of heat capacity anomaly, T_a , and λ -peak temperature, T_c , obtained from specific heat capacity, C_p , in Fig.3(b) are 1210 and 1560 K, respectively. However, available experimental data on specific heat capacity are restricted to temperatures below 1125 K [66–68], and a λ -peak in specific heat capacity was not observed experimentally. On the other hand, neutron diffraction experiments [62] indicate that the onset temperature of lithium disorder, characterized by a rapid increase in the fraction of lithium atoms leaving their regular sites, occurs at approximately 1200 K. This onset temperature of lithium disorder reported by neutron diffraction experiments corresponds to the onset temperature of the heat capacity anomaly, $T_a = 1210$ K, computed in the present MLMD calculation. To calculate the self-diffusion constant, we conducted NVE simulations with a 0.5 fs time step and a total simulation time of 200 ps at various temperatures using the lattice constants previously obtained in the NPT ensemble. Figure 3(c) shows the Arrhenius plot of the self-diffusion constant, $D(T)$, of lithium atom obtained from the slope of the mean square displacement. The Arrhenius plot of $D(T)$ exhibits the downward bending above the T_c .

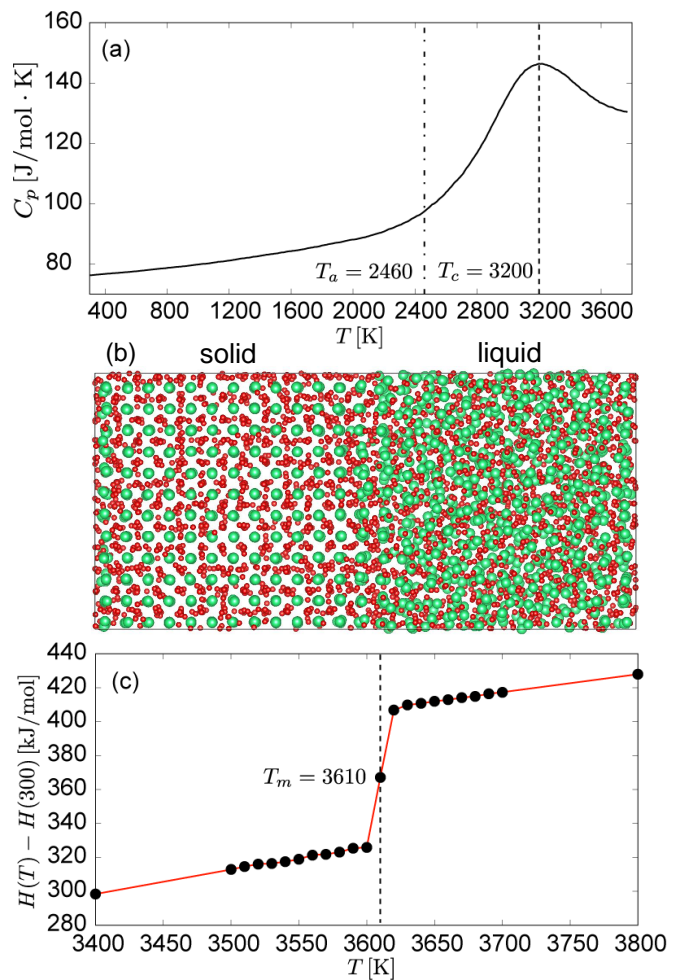


FIG. 2. The thermal properties of ThO_2 obtained by MLMD. (a) Molar specific heat capacity of ThO_2 computed by MLMD. The dashed line denotes the peak position of C_p (λ -peak temperature T_c). The dashed-dot line represents the onset temperature of heat capacity anomaly T_a , (b) $6 \times 6 \times 12$ supercell including solid (left) and liquid phase (right) for two-phase simulation. Green and red balls represent thorium and oxygen atoms, respectively (c) Temperature dependence of the enthalpy of ThO_2 obtained by the two-phase simulation approach using MLMD.

The activation energy of lithium diffusion, E_{AE} , in the range $1000 \text{ K} \leq T < T_c$ using the Arrhenius fitting, $D(T) = D_0 \exp(-E_{AE}/k_B T)$, become 2.44 eV, which well agree with experimental value, 2.52 eV [69]. We also evaluated the formation energy of a Frenkel pair defect, consisting of a lithium interstitial at a 4b position and a vacancy at an 8c position, using structural optimization. The Frenkel pair defect formation energy, E_{FP} , closely matches experimental data, as shown in Table III. The melting point obtained from the present MLMD simulations is in excellent agreement with the experimental melting point (1711 K), as shown in Fig.3 and Table III.

The results demonstrate that the MLMD simulations

using the Li₂O-MLP accurately reproduce the thermal properties of Li₂O. Although the λ -peak in specific heat capacity of Li₂O is not reported experimentally, the λ -peak temperature, T_c , obtained by MLMD is likely reasonable, as the MLMD results agree well with other experimental data, including the melting point. However, it may be difficult to observe the λ -peak in the specific heat capacity of Li₂O clearly in experiments. The melting point and λ -peak temperature predicted by the MLMD simulation are very close, and the λ -peak may be hidden by the jump of specific heat capacity due to the melting of Li₂O.

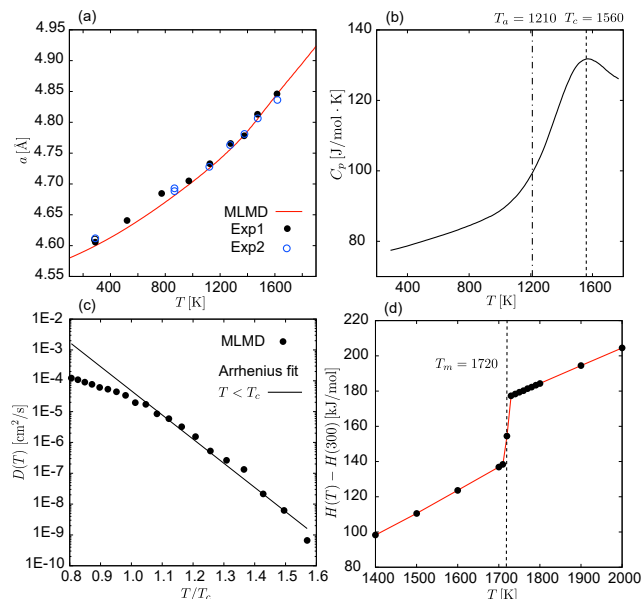


FIG. 3. The thermal properties of Li₂O obtained by MLMD. (a) Temperature dependence of the lattice constant. The solid line represents the results obtained by MLMD, while the filled and open circles represent experimental results (Exp1 [64], Exp2 [62]). (b) Molar specific heat capacity (C_p) computed by MLMD. The dashed line denotes the peak position of C_p (λ -peak temperature T_c). The dashed-dot line represents the onset temperature of heat capacity anomaly T_a , (c) Arrhenius plot of the self-diffusion constant for lithium atom (filled circles). The solid and dashed lines are the results of Arrhenius fitting below and above the transition temperature T_c . (d) Temperature dependence of the enthalpy obtained by two-phase simulation approach using MLMD.

TABLE III. Computed and experimental properties of Li₂O. The lattice constant $L(T)$ at 300 K, the ACLTE in the range from 300 to 1280K, the onset temperature of heat capacity anomaly T_a , λ -peak temperature T_c , the activation energy of lithium diffusion E_{AE} in the range $1000 \text{ K} \leq T < T_c$, the Frenkel pair formation energy E_{FP} , and the melting point T_m are summarized.

	MLMD	Exp.
$L(300\text{K})$ [Å]	4.601	4.610[62], 4.628[63]
ACLTE [10^{-6}K^{-1}]	34.01	33.6[65]
T_a [K]	1210	1200 [62]
T_c [K]	1560	
E_{AE} [eV]	2.44	2.52 [69]
E_{FP} [eV]	2.29	2.10[62], 2.6[70]
T_m [K]	1720	1711 [71]

B. Characterization of the specific heat anomalies of ThO₂ and Li₂O by local order parameter

We have demonstrated that MLMD simulations are reliable for discussing the high-temperature properties of ThO₂ and Li₂O. Using the trajectories obtained from MLMD, we analyze the specific heat anomalies of ThO₂ and Li₂O. We focus on the similarities between the specific heat anomalies of (anti-)fluorite structures and the liquid-liquid phase transitions in network-forming liquids, such as supercooled water (H₂O) and liquid silica (SiO₂) [37–39]. These network-forming liquids also exhibit a λ -peak in specific heat capacity and bending in the Arrhenius plot of the self-diffusion constant at the transition temperature. The liquid-liquid transitions in these network-forming liquids are characterized by local symmetry breaking in their atomic arrangements. The local tetrahedral structures formed by oxygen atoms in supercooled water and silicon atoms in liquid silica play a key role in defining their liquid-liquid transitions [72–75]. Drawing an analogy between liquid-liquid phase transitions and the specific heat anomalies of (anti-)fluorite structures, we focus on the local atomic configurations of oxygen atoms in ThO₂ and lithium atoms in Li₂O. The octahedral structure, consisting of six nearest-neighboring atoms surrounding a central atom, can be considered the minimal local ordered structure of the sublattice in (anti-)fluorite structures (see Fig.1). To quantify this local order, we define the local octahedral order parameter as

$$Q_i = 1 - \frac{1}{8} \sum_{j \in 6\text{NN}_i} \sum_{k \in 4\text{NN}_j} \cos^2 \phi_{ijk}, \quad (6)$$

where ϕ_{ijk} denotes the internal angle of the octahedron. The summation over $j \in 6\text{NN}_i$ accounts for the six nearest neighboring atoms relative to the i -th atom, while the $k \in 4\text{NN}_j$ represents the four nearest neighboring atoms within the 6NN_i group from the j -th atom. The order parameter Q_i equals one when the six nearest neighboring atoms of the i -th atom form an ideal octahedral structure, characterized by internal angles of 90 degrees. The

expectation value of the order parameter becomes zero, $\langle Q_i \rangle_{\text{rand}} = 0$, if the internal angles, ϕ_{ijk} , are completely random.

We calculated the distribution of the local octahedral order parameter, $P(Q)$, from the trajectories of the MLMD, as shown in Fig.4(a) and 4(b). At 300 K, $P(Q)$ exhibits a sharp peak, $Q_1 \simeq 1$, indicative of the perfect local octahedral order of oxygen (lithium) atoms in ThO_2 (Li_2O). As the temperature increases, the height of the Q_1 -peak decreases due to the disruption of the octahedral atomic arrangement caused by large thermal vibrations. Additionally, new peaks representing defective local structures emerge in the low- Q region at higher temperatures. The low Q -peaks becomes predominant near the λ -transition temperature, T_c . This behavior closely resembles the change in the local tetrahedral order parameter for the liquid-liquid transition of super-cooled water and liquid silica [73–76]. Comparing the temperature change of the local tetrahedral order parameter in these network-forming liquids, the distributions of the local octahedral order parameter in the low Q region show two peaks, Q_2 and Q_3 , in the present (anti-)fluorite systems. The position of the Q_3 -peak is nearly identical to the peak position of the liquid state (see dashed lines in Fig.4(a) and Fig.4(b)). Interestingly, two peaks, Q_2 and Q_3 , merge into a single low Q -peak at T_c , indicating the qualitative changes of the defect structures in ThO_2 and Li_2O associated with the λ -transition.

To elucidate the significance of each peak, we computed the angle and atomic spatial distributions of the six nearest neighboring (6NN) atoms around a central atom with Q values belonging to the Q_1 -, Q_2 -, and Q_3 -peak regions. The Q_1 -, Q_2 - and Q_3 -peak regions were assigned on the basis of the local minimum values of $P(Q)$ at the onset temperature of heat capacity anomaly, T_a . The Q_1 -peak region is $0.755 < Q \leq 1$, the Q_2 peak region is $0.535 < Q \leq 0.755$, and the Q_3 -peak region is $Q \leq 0.535$, which are common for both ThO_2 and Li_2O . Figure 5(a)-(c) show the angle distributions belonging to the Q_1 -, Q_2 - and Q_3 -peak regions for Li_2O . A single peak is observed at 90 degrees in the angle distribution for the Q_1 peak, representing the ideal octahedral structure, as shown in Fig.5(a). For the angle distribution of the Q_2 peak, the distribution more broadens, and a small peak appears between 40 and 60 degrees. This small peak is attributed to the atomic arrangement where the 6NN atoms partially occupy either the next-nearest neighboring 8c (NNN-8c) positions or the interstitial 4b positions (see the lower panel of Fig.5(b)). This is because, if a 6NN atom partially occupies a position near NNN-8c or 4b, the angle becomes approximately 40 to 60 degrees. Indeed, the occupancy of both the NNN-8c and interstitial 4b positions are confirmed in the atomic spatial distribution in Fig.5(b). Thermal vibrations at high temperatures induce significant anharmonicity, disrupting the octahedral arrangement of the 6NN atoms. The presence of 4b occupancies confirms that the Q_2 -peak reflects a lattice defect-like local structure (a Frenkel pair defect-like

local structure). In the angle distribution for the Q_3 peak, the peak between 40 and 60 degrees accounts for a more significant proportion than the distribution of the Q_2 peak. This increase in the peak corresponds to cases where multiple NNN-8c positions are included among the 6NN atoms (see the lower-left panel of Fig.5(b)) or to disordered local structures that are difficult to assign to specific Wyckoff positions (see the lower-middle panel of Fig.5(b)). The atomic spatial distribution for the Q_3 -peak also has local maximums at the NN-8c and NNN-8c position, similar to the Q_2 -peak distribution, but the 4b position does not become a local maximum. Therefore, the Q_3 peak is considered to represent a local defect structure qualitatively different from the lattice defect-like local structure of the Q_2 peak. The position of the Q_3 peak in $P(Q)$ is nearly identical to the peak position of the liquid state (see dashed lines in Fig.4(b)), and its angular distribution, $P_{6\text{NN}}(\theta)$, closely resembles that of the liquid phase (see dashed lines in Fig.5(c)). Thus, the Q_3 -peak represents the disordered local structure resembling the local structure of the liquid phase.

We have shown that the mobile atoms in ThO_2 and Li_2O have three characteristic local structures at high-temperature: the octahedral local structure (Q_1), the lattice defect-like local structure (Q_2), and the liquid-like local structure (Q_3). The Q_2 and Q_3 peaks merge into a single low- Q peak at T_c , indicating a qualitative change in the mobility of atoms in ThO_2 and Li_2O . We computed the one-particle atomic distribution of mobile atoms,

$$p_A(\mathbf{x}) = \frac{1}{N_A} \left\langle \sum_i^{N_A} \delta(\mathbf{x} - \mathbf{x}_i) \right\rangle, \quad (7)$$

where $\langle \cdot \rangle$ means thermal average, and $A = \text{O}, \text{Li}$. From the $p_A(\mathbf{x})$, we calculate the effective one-particle effective potentials for the [111] direction from 8c to 4b position as

$$V_A^{(\text{eff})}(8c \rightarrow 4b) \equiv -k_B T \ln \left(\frac{p_A(\mathbf{x} = 8c \rightarrow 4b)}{p_A(\mathbf{x} = 8c)} \right), \quad (8)$$

where k_B is boltzmann constant. As shown in Fig.6.(a) and (b), $V_A^{(\text{eff})}(8c \rightarrow 4b)$ has a local minimum at the 4b position at low temperature, while the local minimum disappears near T_c . The 4b position does not become a metastable state above T_c , indicating that mobile atoms no longer stagnate in the interstitial 4b position. This result corresponds to the fusion of the Q_2 -peak (lattice defect-like local structure) and the Q_3 -peak (liquid-like local structure) above T_c . The sub-lattice formed by mobile atoms melts and the defective local structure becomes close to the liquid-like structure above T_c . The bending of the self-diffusion constant of mobile atoms at T_c is considered due to the transition of the local structure from the lattice defect-like local structure to the liquid-like one above T_c .

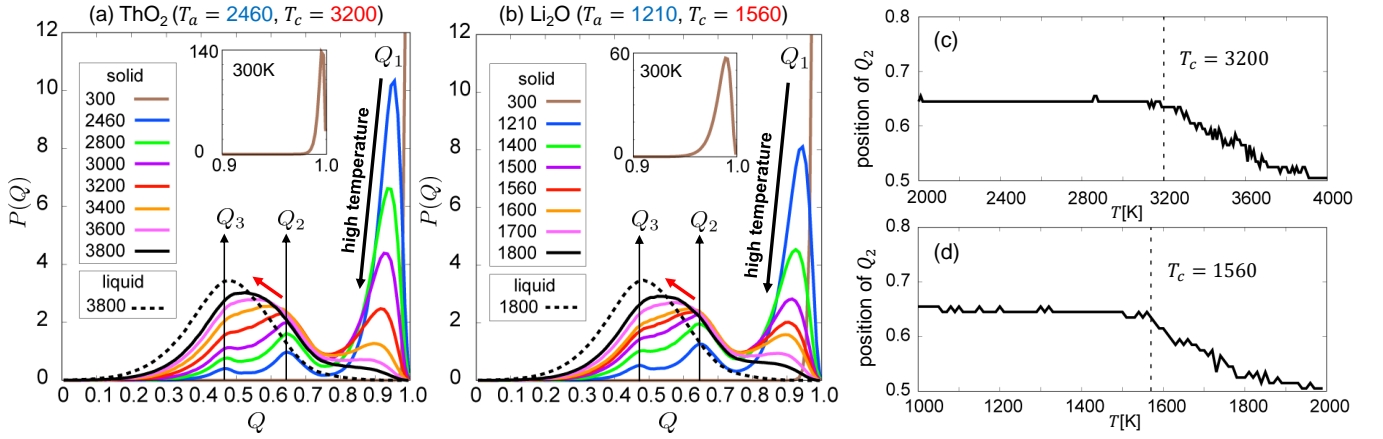


FIG. 4. (a) and (b): The distribution of the local octahedral order parameter for the oxygen atoms in ThO_2 and lithium atoms in Li_2O , $P(Q)$, for ThO_2 and Li_2O , respectively. The solid lines represent $P(Q)$ for the solid phase, while the dashed lines denote the liquid phase. The insets show the results at 300 K for clarity. (c) and (d) show the change of the position of Q_2 -peak in $P(Q)$ for ThO_2 and Li_2O , respectively.

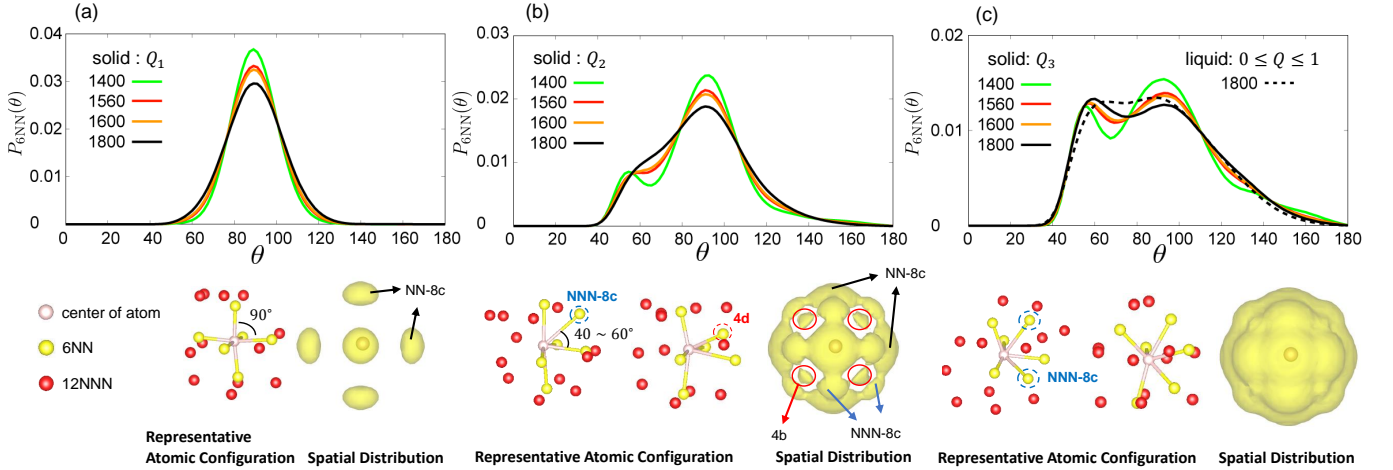


FIG. 5. The angle distribution of the six nearest neighboring (6NN) lithium atoms, $P_{6\text{NN}}(\theta)$, relative to a central lithium atom in Li_2O . (a)-(c) show $P_{6\text{NN}}(\theta)$ corresponding to the local atomic arrangements with octahedral order parameter values at the following ranges: Q_1 ($0.755 < Q \leq 1$), Q_2 ($0.535 < Q \leq 0.755$), Q_3 ($Q \leq 0.535$), respectively. For comparison, the angle distribution for the liquid phase is also shown in panel (c) (dashed line). Here, the angle distribution for the liquid phase is plotted across the range, $0 \leq Q \leq 1$. The lower panels illustrate representative atomic configurations and spatial distributions for each Q -region. The white, yellow, and red balls represent the center of the lithium atom, the six nearest neighboring (6NN) lithium atoms, and the twelve next-nearest neighboring (12NNN) lithium atoms, respectively. The spatial distributions denote the distributions of 6NN lithium atoms relative to the center of the lithium atom. The configurations and spatial distributions are obtained from the MLMD trajectory of lithium for Li_2O at 1600 K.

IV. CONCLUSION

We have performed MLMD simulations to explore the high-temperature properties of ThO_2 and Li_2O , which possess fluorite and anti-fluorite structures, respectively. Our results show that the MLMD simulations accurately reproduce the thermal properties reported in experiments. The MLMD simulations predicted a λ -transition temperature of 1560 K for Li_2O , a value that has not been

experimentally reported. The computed λ -transition temperature is considered reasonable since the MLMD results well reproduced the other reported experimental data. However, the predicted λ -transition temperature is close to the experimental melting point of 1711 K. This result implies that observing a distinct λ -peak in specific heat capacity experimentally may be difficult due to the jump in specific heat capacity associated with the melting of Li_2O .

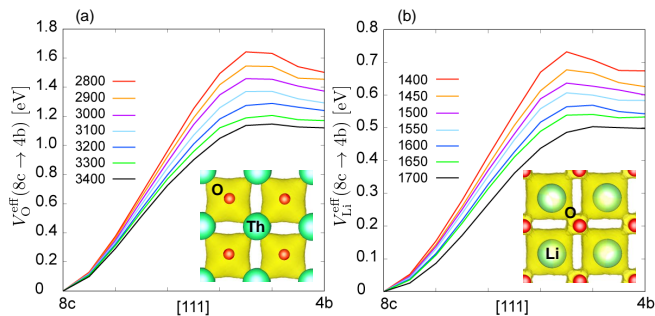


FIG. 6. (a) and (b) represent effective one-particle potential energies of oxygen and lithium atoms in ThO_2 and Li_2O from the $[111]$ direction from 8c to 4b position.

Using the MLMD trajectories, we investigated the heat anomalies of ThO_2 and Li_2O from the perspective of local symmetry breaking, a concept proposed to explain the liquid-liquid transition in network-forming liquids. We introduced the local octahedral order parameter and analyzed how its distribution changes with increasing temperature. The changes in these distributions with rising temperature closely resemble the changes observed in the distribution of the tetrahedral order parameter in super-cooled water and liquid silica. The local octahedral or-

der parameter revealed two distinct defective peaks below the transition temperature. The first peak corresponds to a lattice defect-like local structure, while the second corresponds to a liquid-like local structure. These two peaks merge into a single peak at λ -transition temperature, and mobile atoms no longer stagnate in interstitial 4b positions. The sub-lattice character of mobile atoms disappears, and the liquid-like local structure becomes dominant above the transition temperature.

ACKNOWLEDGEMENTS

K.K. was supported by JSPS KAKENHI Grants Number 24K08574. H.N. was supported by JSPS KAKENHI Grants Number 23K04637. These calculations were mainly performed on the supercomputing system HPE SGI8600 in the Japan Atomic Energy Agency. We would thank all staff members of CCSE for computational support. We also partially used the computational resources of Fujitsu PRIMERGY CX400M1/CX2550M5 (Oakbridge-CX), Fujitsu PRIMEHPC FX1000, FUJITSU PRIMERGY GX2570 (Wisteria/BDEC-01), and “mdx: a platform for the data-driven future” supported by “Joint Usage/Research Center for Interdisciplinary Large-scale Information Infrastructures” in Japan (Project ID: jh230069). The crystal structures were drawn with VESTA [77].

-
- [1] J. Van Der Laan, H. Kawamura, N. Roux, and D. Yamaki, Ceramic breeder research and development: progress and focus, *Journal of nuclear materials* **283**, 99 (2000).
- [2] S. Potashnikov, A. Boyarchenkov, K. Nekrasov, and A. Y. Kupryazhkin, High-precision molecular dynamics simulation of uo_2 - puo_2 : Pair potentials comparison in uo_2 , *Journal of Nuclear Materials* **419**, 217 (2011).
- [3] M. W. D. Cooper, M. J. D. Rushton, and R. W. Grimes, A many-body potential approach to modelling the thermomechanical properties of actinide oxides, *Journal of Physics: Condensed Matter* **26**, 105401 (2014).
- [4] M. W. Cooper, S. T. Murphy, P. C. Fossati, M. J. Rushton, and R. W. Grimes, Thermophysical and anion diffusion properties of $(\text{u x}, \text{th}1-x)\text{o}_2$, *Proceedings of the Royal Society A: Mathematical, Physical and Engineering Sciences* **470**, 20140427 (2014).
- [5] C. Galvin, M. Cooper, M. Rushton, and R. Grimes, Thermophysical properties and oxygen transport in $(\text{thx}, \text{pu}1-x)\text{o}_2$, *Scientific Reports* **6**, 36024 (2016).
- [6] M. Hayoun, M. Meyer, and A. Denieport, Complex atomic-diffusion mechanism in ionic superconductors: The case of the lithium-oxide antiperovskite, *Acta materialia* **53**, 2867 (2005).
- [7] T. Oda and S. Tanaka, Modeling of li diffusivity in li_2o by molecular dynamics simulation, *Journal of nuclear materials* **386**, 1087 (2009).
- [8] R. Asahi, C. M. Freeman, P. Saxe, and E. Wimmer, Thermal expansion, diffusion and melting of li_2o using a compact forcefield derived from ab initio molecular dynamics, *Modelling and Simulation in Materials Science and Engineering* **22**, 075009 (2014).
- [9] M. Y. Lavrentiev, N. Allan, and C. Wragg, Lithium oxide: a quantum-corrected and classical monte carlo study, *Physical Chemistry Chemical Physics* **21**, 14964 (2019).
- [10] H. Nakamura, M. Machida, and M. Kato, First-principles calculation of phonon and schottky heat capacities of plutonium dioxide, *Journal of the Physical Society of Japan* **84**, 053602 (2015).
- [11] B. Szpunar and J. Szpunar, Theoretical investigation of structural and thermo-mechanical properties of thoria up to 3300 k temperature, *Solid state sciences* **36**, 35 (2014).
- [12] B. Szpunar, J. Szpunar, and K.-S. Sim, Theoretical investigation of structural and thermo-mechanical properties of thoria, *Journal of Physics and Chemistry of Solids* **90**, 114 (2016).
- [13] H. Nakamura and M. Machida, High-temperature properties of thorium dioxide: A first-principles molecular dynamics study, *Journal of Nuclear Materials* **478**, 56 (2016).
- [14] M. Gupta, B. Singh, P. Goel, R. Mittal, S. Rols, and S. Chaplot, Lithium diffusion in li_2x ($\text{x} = \text{o}, \text{s}$, and se): Ab initio simulations and inelastic neutron scattering measurements, *Physical Review B* **99**, 224304 (2019).
- [15] A. Jaberi, J. Song, and R. Gauvin, Study of lithium transport in li_2o component of the solid electrolyte interphase in lithium-ion batteries, *Computational Materials Science* **237**, 112914 (2024).

- [16] J. Behler and M. Parrinello, Generalized neural-network representation of high-dimensional potential-energy surfaces, *Phys. Rev. Lett.* **98**, 146401 (2007).
- [17] A. P. Bartók, M. C. Payne, R. Kondor, and G. Csányi, Gaussian approximation potentials: The accuracy of quantum mechanics, without the electrons, *Phys. Rev. Lett.* **104**, 136403 (2010).
- [18] J. Behler, Constructing high-dimensional neural network potentials: A tutorial review, *International Journal of Quantum Chemistry* **115**, 1032 (2015).
- [19] A. P. Bartók and G. Csányi, Gaussian approximation potentials: A brief tutorial introduction, *International Journal of Quantum Chemistry* **115**, 1051 (2015).
- [20] K. Kobayashi, M. Okumura, H. Nakamura, M. Itakura, M. Machida, S. Urata, and K. Suzuya, Machine learning molecular dynamics reveals the structural origin of the first sharp diffraction peak in high-density silica glasses, *Scientific Reports* **13**, 18721 (2023).
- [21] Y. Nagai, Y. Iwasaki, K. Kitahara, Y. Takagiwa, K. Kimura, and M. Shiga, High-temperature atomic diffusion and specific heat in quasicrystals, *Physical Review Letters* **132**, 196301 (2024).
- [22] S. Urata, M. Bertani, and A. Pedone, Applications of machine-learning interatomic potentials for modeling ceramics, glass, and electrolytes: A review, *Journal of the American Ceramic Society* (2024).
- [23] K. Kobayashi, M. Okumura, H. Nakamura, M. Itakura, M. Machida, and M. W. Cooper, Machine learning molecular dynamics simulations toward exploration of high-temperature properties of nuclear fuel materials: Case study of thorium dioxide, *Scientific reports* **12**, 9808 (2022).
- [24] E. T. Dubois, J. Tranchida, J. Bouchet, and J.-B. Maillet, Atomistic simulations of nuclear fuel UO_2 with machine learning interatomic potentials, *Physical Review Materials* **8**, 025402 (2024).
- [25] E. Stippell, L. Alzate-Vargas, K. N. Subedi, R. M. Tutchtun, M. W. Cooper, S. Tretiak, T. Gibson, and R. A. Messerly, Building a dft+ u machine learning interatomic potential for uranium dioxide, *Artificial Intelligence Chemistry* **2**, 100042 (2024).
- [26] A. S. Dworkin and M. A. Bredig, Diffuse transition and melting in fluorite and antiferite type of compounds. heat content of potassium sulfide from 298 to 1260-degree.k, *The Journal of Physical Chemistry* **72**, 1277 (1968).
- [27] M. T. Hutchings, K. Clausen, M. H. Dickens, W. Hayes, J. K. Kjems, P. G. Schnabel, and C. Smith, Investigation of thermally induced anion disorder in fluorites using neutron scattering techniques, *Journal of Physics C: Solid State Physics* **17**, 3903 (1984).
- [28] K. Clausen, W. Hayes, J. E. Macdonald, R. Osborn, and M. T. Hutchings, Observation of oxygen frenkel disorder in uranium dioxide above 2000 k by use of neutron-scattering techniques, *Phys. Rev. Lett.* **52**, 1238 (1984).
- [29] S. Hull, Superionics: crystal structures and conduction processes, *Reports on Progress in Physics* **67**, 1233 (2004).
- [30] A. Annamareddy and J. Eapen, Low Dimensional Stringlike Relaxation Underpins Superionic Conduction in Fluorites and Related Structures, *Scientific Reports* **7**, 1 (2017).
- [31] H. Zhang, X. Wang, A. Chremos, and J. F. Douglas, Superionic UO_2 : A model anharmonic crystalline material, *The Journal of Chemical Physics* **150**, 174506 (2019).
- [32] C. Donati, J. F. Douglas, W. Kob, S. J. Plimpton, P. H. Poole, and S. C. Glotzer, Stringlike cooperative motion in a supercooled liquid, *Physical review letters* **80**, 2338 (1998).
- [33] C. Derrington and M. O'KEEFFE, Anion conductivity and disorder in lead fluoride, *Nature Physical Science* **246**, 44 (1973).
- [34] V. Carr, A. Chadwick, and R. Saghafian, The electrical conductivity of PbF_2 and $SrCl_2$ crystals at high temperatures, *Journal of Physics C: Solid State Physics* **11**, L637 (1978).
- [35] G. Imbalzano, A. Anelli, D. Giofré, S. Klees, J. Behler, and M. Ceriotti, Automatic selection of atomic fingerprints and reference configurations for machine-learning potentials, *The Journal of Chemical Physics* **148**, 241730 (2018).
- [36] R. K. Cersonsky, B. A. Helfrecht, E. A. Engel, S. Klavinek, and M. Ceriotti, Improving sample and feature selection with principal covariates regression, *Machine Learning: Science and Technology* **2**, 035038 (2021).
- [37] H. Tanaka, Simple view of waterlike anomalies of atomic liquids with directional bonding, *Physical Review B* **66**, 064202 (2002).
- [38] C. Angell, R. Bressel, M. Hemmati, E. Sare, and J. Tucker, Water and its anomalies in perspective: Tetrahedral liquids with and without liquid-liquid phase transitions. invited lecture, *Physical Chemistry Chemical Physics* **2**, 1559 (2000).
- [39] I. Saika-Voivod, P. H. Poole, and F. Sciortino, Fragile-to-strong transition and polyamorphism in the energy landscape of liquid silica, *Nature* **412**, 514 (2001).
- [40] S. Plimpton, Fast parallel algorithms for short-range molecular dynamics, *Journal of Computational Physics* **117**, 1 (1995).
- [41] G. Kresse and J. Hafner, Ab initio molecular dynamics for liquid metals, *Physical Review B* **47**, 558 (1993).
- [42] G. Kresse and J. Furthmüller, Efficient iterative schemes for ab initio total-energy calculations using a plane-wave basis set, *Physical review B* **54**, 11169 (1996).
- [43] J. P. Perdew, Accurate density functional for the energy: Real-space cutoff of the gradient expansion for the exchange hole, *Physical Review Letters* **55**, 1665 (1985).
- [44] J. Sun, A. Ruzsinszky, and J. P. Perdew, Strongly constrained and appropriately normed semilocal density functional, *Physical Review Letters* **115**, 036402 (2015).
- [45] A. Singraber, J. Behler, and C. Dellago, Library-based lammps implementation of high-dimensional neural network potentials, *Journal of Chemical Theory and Computation* **15**, 1827 (2019).
- [46] V. Botu and R. Ramprasad, Adaptive machine learning framework to accelerate *ab initio* molecular dynamics, *International Journal of Quantum Chemistry* **115**, 1074 (2015).
- [47] Z. Li, J. R. Kermode, and A. De Vita, Molecular dynamics with on-the-fly machine learning of quantum-mechanical forces, *Phys. Rev. Lett.* **114**, 096405 (2015).
- [48] M. Gastegger, J. Behler, and P. Marquetand, Machine learning molecular dynamics for the simulation of infrared spectra, *Chem. Sci.* **8**, 6924 (2017).
- [49] T. L. Jacobsen, M. S. Jørgensen, and B. Hammer, On-the-fly machine learning of atomic potential in density functional theory structure optimization, *Phys. Rev. Lett.* **120**, 026102 (2018).

- [50] W. Li and Y. Ando, Dependence of a cooling rate on structural and vibrational properties of amorphous silicon: A neural network potential-based molecular dynamics study, *The Journal of Chemical Physics* **151**, 114101 (2019).
- [51] A. R. Tan, S. Urata, S. Goldman, J. C. Dietschreit, and R. Gómez-Bombarelli, Single-model uncertainty quantification in neural network potentials does not consistently outperform model ensembles, *npj Computational Materials* **9**, 225 (2023).
- [52] R. Z. Khaliullin, H. Eshet, T. D. Kühne, J. Behler, and M. Parrinello, Nucleation mechanism for the direct graphite-to-diamond phase transition, *Nature Materials* **10**, 693 (2011).
- [53] T. Morawietz, A. Singraber, C. Dellago, and J. Behler, How van der Waals interactions determine the unique properties of water, *Proceedings of the National Academy of Sciences* **113**, 8368 (2016).
- [54] N. Artrith and A. Urban, An implementation of artificial neural-network potentials for atomistic materials simulations: Performance for TiO₂, *Computational Materials Science* **114**, 135 (2016).
- [55] S. Wolf, *The chemistry of the actinide and transactinide elements* (2006) pp. 3273–3338.
- [56] A. Momin, E. Mirza, and M. Mathews, High temperature x-ray diffractometric studies on the lattice thermal expansion behaviour of UO₂, ThO₂ and (U_{0.2}Th_{0.8})O₂ doped with fission product oxides, *Journal of Nuclear Materials* **185**, 308 (1991).
- [57] P. Rodriguez and C. Sundaram, Nuclear and materials aspects of the thorium fuel cycle, *Journal of Nuclear Materials* **100**, 227 (1981).
- [58] *Thermophysical Properties Database of Materials for Light Water Reactors and Heavy Water Reactors*, TECDOC Series No. 1496 (INTERNATIONAL ATOMIC ENERGY AGENCY, Vienna, 2006).
- [59] D. Fischer, J. Fink, and L. Leibowitz, Enthalpy of thorium dioxide to 3400 K, *Journal of Nuclear Materials* **102**, 220 (1981).
- [60] C. Ronchi and J. Hiernaut, Experimental measurement of pre-melting and melting of thorium dioxide, *Journal of Alloys and Compounds* **240**, 179 (1996).
- [61] J. Eapen and A. Annamareddy, Entropic crossovers in superionic fluorites from specific heat, *Ionics* **23**, 1043 (2017).
- [62] T. W. D. Farley, W. Hayes, S. Hull, M. T. Hutchings, and M. Vrtis, Investigation of thermally induced Li⁺ ion disorder in Li₂O using neutron diffraction, *Journal of Physics: Condensed Matter* **3**, 4761 (1991).
- [63] J. Robert, U. Wilhelm, and G. Wilhelm, Über mischkristalle, die ein zweifach und ein dreifach geladenes anion enthalten, *Zeitschrift für anorganische und allgemeine Chemie* **292**, 71 (1957).
- [64] S. Hull, T. W. D. Farley, W. Hayes, and M. T. Hutchings, The elastic properties of lithium oxide and their variation with temperature, *Journal of Nuclear Materials* **160**, 125 (1988).
- [65] T. Kurasawa, T. Takahashi, K. Noda, H. Takeshita, S. Nasu, and H. Watanabe, Thermal expansion of lithium oxide, *Journal of Nuclear Materials* **107**, 334 (1982).
- [66] C. H. Shomate and A. J. Cohen, High temperature heat content and entropy of lithium oxide and lithium hydroxide, *Journal of the American Chemical Society* **77**, 285 (1955).
- [67] I. Barin, O. Knacke, and O. Kubaschewski, *Thermochemical properties of inorganic substances: supplement* (Springer Science & Business Media, 2013).
- [68] T. Tanifuji and S. Nasu, Heat capacity and thermal decomposition of lithium peroxide, *Journal of Nuclear Materials* **87**, 189 (1979).
- [69] Y. Oishi, Y. Kamei, M. Akiyama, and T. Yanagi, Self-diffusion coefficient of lithium in lithium oxide, *Journal of Nuclear Materials* **87**, 341 (1979).
- [70] A. V. Chadwick, Electrical conductivity measurements of ionic solids, *Philosophical Magazine A* **64**, 983 (1991).
- [71] M. S. ORTMAN and E. M. LARSEN, Preparation, characterization, and melting point of high-purity lithium oxide, *Journal of the American Ceramic Society* **66**, 645 (1983).
- [72] J. R. Errington and P. G. Debenedetti, Relationship between structural order and the anomalies of liquid water, *Nature* **409**, 318 (2001).
- [73] P. Kumar, S. V. Buldyrev, and H. E. Stanley, A tetrahedral entropy for water, *Proceedings of the National Academy of Sciences* **106**, 22130 (2009).
- [74] J. Geske, B. Drossel, and M. Vogel, Fragile-to-strong transition in liquid silica, *AIP Advances* **6** (2016).
- [75] R. Shi and H. Tanaka, Impact of local symmetry breaking on the physical properties of tetrahedral liquids, *Proceedings of the National Academy of Sciences* **115**, 1980 (2018).
- [76] R. Shi and H. Tanaka, Distinct signature of local tetrahedral ordering in the scattering function of covalent liquids and glasses, *Science advances* **5**, eaav3194 (2019).
- [77] K. Momma and F. Izumi, VESTA: a three-dimensional visualization system for electronic and structural analysis, *Journal of Applied Crystallography* **41**, 653 (2008).